Journal of Materials Chemistry C

ROYAL SOCIETY OF CHEMISTRY

PAPER

View Article Online
View Journal

Cite this: DOI: 10.1039/d2tc04418h

Quantification of energy transfer processes from crystalline silicon to erbium†

Huan Liu,[a] Ulrich Kentsch,[b] Fangyu Yue,[c] Abdelmadjid Mesli[a] and Yaping Dan *[a]

Received 18th October 2022,
Accepted 4th January 2023

DOI: 10.1039/d2tc04418h

rsc.li/materials-c

Erbium-implanted silicon is considered as a promising system to realize electrically pumped light sources at the communication band due to the stable luminescence of Er ions at 1536 nm. However, this system suffers from an extremely low luminescence efficiency at room temperature. Quantitatively, understanding the energy transfer processes in the system is critical to improving the Er luminescence efficiency, which unfortunately remains ambiguous. In this article, we managed to establish a complete methodology that can quantitatively describe the energy transfer processes from Si to Er. We first employed the Kohlrausch's function to analyze the transient photoluminescence (PL) of Er in silicon at different temperatures, from which we found the emission flux and effective decay rate of excited Er ions in steady state. These extracted parameters were used in the widely accepted energy transfer processes to analyze Er PL behaviors as a function of temperature (80–300 K) and excitation power. Interestingly, we managed to quantitatively find almost all important physical parameters of the energy transfer process including the energy transfer efficiency from Er-related defects to Er ions (21.6% at room temperature), the PhotoLuminescence Quantum Yield (PLQY, 0.45% at room temperature) and a record high optically active Er concentration (2×10^{19} cm^{-3}). In this system, high defect density, rather than severe energy back-transfer process, becomes the limiting factor for efficient Er emission. Further careful analysis indicates that the Er/O/B-doped silicon has a potential to reach a PLQY of 3.5% if the defects in the Si bandgap are properly passivated.

Introduction

Erbium is a common rare earth element which is widely used in active photonic devices, such as the Erbium-Doped Fiber Amplifier (EDFA) and Erbium-Doped Fiber Laser (EDFL). Although erbium has long been applied in the EDFA and EDFL, the integration of erbium with silicon[1–4] to make an efficient electrically pumped light source is quite challenging due to the low solubility of Er in Si ($\sim 1 \times 10^{16}$ cm^{-3})[5] and strong competitive processes at room temperature,[6] including the thermal-quenching effect, free-carrier Auger effect, *etc.* Thanks to the non-equilibrium ion implantation method followed by thermal annealing techniques, the concentration of erbium in silicon can be enhanced to the order of 1×10^{20} cm^{-3}.[4] Unfortunately, the concentration of the optically active Er dopant remains low. Previous work reported that co-dopants with large electronegative atoms like oxygen (O) and fluorine (F) can help increase the optically active concentration of Er which is still below 1×10^{18} cm^{-3}.[5,7] Interestingly, the introduction of boron into Er/O-implanted silicon was observed to suppress the free-carrier Auger effect.[8] However, the luminescence of Er ions is still quenched about 2–3 orders when the temperature is increased from 4 K to 300 K,[9] known as the thermal quenching effect. Our previous work reported a giant PL enhancement at room temperature when the samples are processed using a so-called "Deep Cooling" (DC) technique.[10] Despite these improvements, experimental observation of net optical gain in an Er:c-Si system is still challenging due to the low optically active Er concentration.[3,11,12] Therefore, it is imperative for us to reopen the "black box" (energy transfer between Er and Si), re-evaluate its efficiency and consider where we are now and along which path we can move forward to realize room-temperature Er:c-Si-based amplifiers.

In this article, a theoretical model is introduced to describe the energy transfer processes after applying the Kohlrausch's function to fit transient PL signals. Based on this model, we found a record high optically active Er concentration of 2×10^{19} cm^{-3} for the boron co-doped Er/O–Si sample. More interestingly, we also

[a] University of Michigan-Shanghai Jiao Tong University Joint Institute, Shanghai Jiao Tong University, Shanghai, 200240, China. E-mail: yaping.dan@sjtu.edu.cn
[b] Institute of Ion Beam Physics and Materials Research, Helmholtz-Zentrum Dresden – Rossendorf, Dresden, 01328, Germany
[c] Key Laboratory of Polar Materials and Devices, Ministry of Education, East China Normal University, Shanghai, 200241, China

† Electronic supplementary information (ESI) available. See DOI: https://doi.org/10.1039/d2tc04418h

found that the forward energy transfer efficiency from Er-Related Defect States (ERDS) to Er ions is as high as 21.6%, implying that a very high internal quantum efficiency for Er-doped Si can be potentially achieved if the Er-Irrelated Defect States (EIDS) in the Si bandgap are properly passivated.

Results and discussion

Intrinsic Si(100) wafers were first implanted with Er, O, and B ions with a uniform doping profile along the implantation direction (parameters listed in the ESI† SI-I). Two types of samples were compared, one with only Er/O implantations and the other contains Er/O/B. For each type, two annealing methods were applied. One is the DC technique that we used before, which can significantly suppress Er precipitation[10] and achieve a much stronger PL emission when the system is without boron doping. The other annealing method is the traditional Solid Phase Epitaxy (SPE), with which, compared with the DC technique, a stronger PL emission was obtained when boron was introduced, and no room temperature PL signal was attainable when there were only Er and O dopants in silicon (without boron). Therefore, after optimization of annealing conditions and dopant ratio (see SI-II, ESI†), three samples were chosen for the investigation.

The simulated uniform distribution was verified by Secondary Ion Mass Spectrometry (SIMS) in the ESI† (see Fig. S1 in SI-I). Clearly, Er, O and B are uniformly distributed from 25 nm to 125 nm below the Si surface at a concentration of 8.7×10^{20} cm^{-3}, 2.0×10^{21} cm^{-3}, and 7.7×10^{19} cm^{-3}, respectively. Note that the ultra-high O concentration near the surface comes from the oxidation of silicon. Since the implantation energies remain unchanged among all samples, the step-like shape of Er/O/B was well preserved. After implantation, D_0 and D_1 were processed using the DC technique as described in our previous work.[10] S_1 was annealed in the Muffle furnace at 1100 °C for 30 minutes (verified to be the best SPE condition, see SI-II, ESI†) in the atmosphere of N_2 to activate the Er.

The photoluminescence (PL) spectrometer (Edinburgh, FLS1000) was used to obtain both the steady-state emission spectrum and time-resolved decay transients of our Er-implanted silicon samples. As shown in Fig. 1a, nearly identical broadband (full-width-half-maximum, FWHM ~40 nm) PL spectra (normed) were obtained from 300 K to 4 K (only two curves are shown). There are two obvious peaks (1536 nm, and 1550 nm), indicated by two arrows. These two PL peaks are commonly attributed to the two distinct optical-active Er sites, just like the observations in the MBE-grown Er:Si systems in previous work[13] as shown in the Fig. 1a bottom panel.

The transient PL dynamics of Er in Si is not a simple exponential, as shown in Fig. 1b. In some previous works,[14–18] double-exponential functions were used to fit the decay curve with each component representing one Er site as shown in Fig. 1a. However, we found that this cognition is not convincing. If the Er PL comes from different Er configurations with slow or fast decay behaviors, large lifetime differences would be expected at different wavelengths, or equivalently, an obvious distortion of the PL spectral shape would be observed at different time slices after the optical pump is turned off. To verify this, Time Evolution Resolved Spectrum (TERS) measurements were

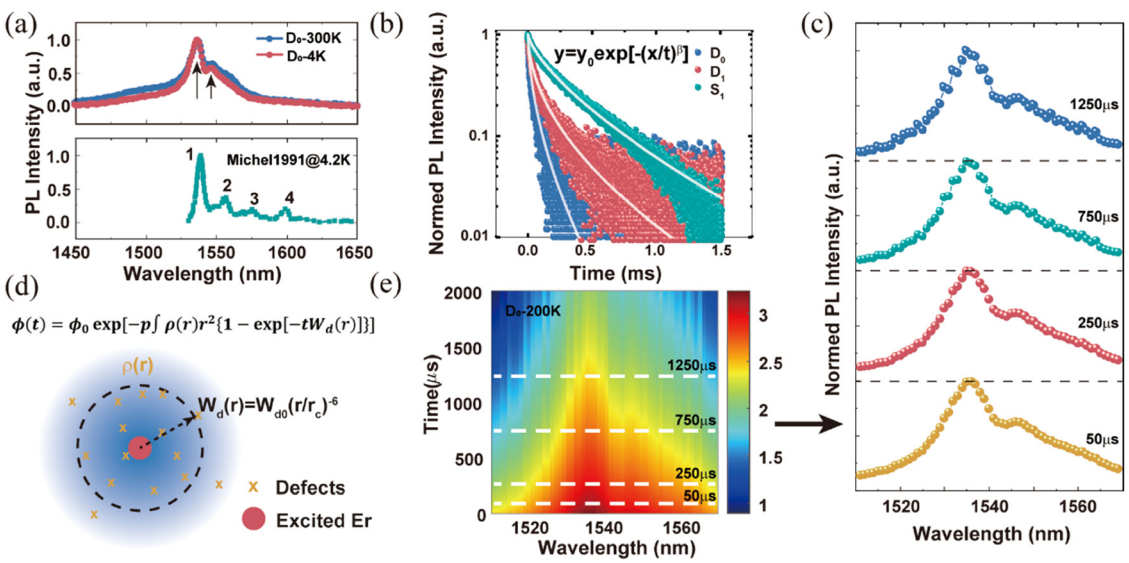

Fig. 1 Basic material properties. (a) The steady-state photoluminescence spectra of our Er/O co-doped sample (D_0) at 4 K and 300 K (up panel) and previously reported Er-implanted silicon at 4.2 K (bottom panel). (b) Decay dynamics of samples D_0, D_1, S_1 at room temperature with the pumping photoflux density of 5.5×10^{18} s^{-1} cm^{-2}. The white solid lines are fitting curves using eqn (1). (c) Normalized PL spectra at different time slices in (b). (d) The schematic 2D diagram of an excited erbium's decay through parallel multi-channel routes with defects density distribution $\rho(R)$. The decay rate of a defect with distance R is $W_d(R)$. The dashed circle represents the characteristic interaction radius for a typical Förster type energy transfer. The expression on the top gives the overall decay shape of this multi-parallel decaying system. (e) Time evolution resolved spectrum (TERS) of sample D_0 at 200 K. The white dashed lines indicate time slices of 50 μs, 250 μs, 750 μs and 1250 μs, respectively.

performed for sample S_1, as shown in Fig. 1c and e. The spectrum line-shape does not change much at different times. Therefore, it is unreasonable to separate fast and slow components in the decay dynamics. Instead, the decay dynamics should be treated as a collective effect from multi-parallel decay paths of excited Er ions. Joseph *et al.*[19] gave a clear mathematical description of the multi-parallel decay picture for an excited particle (see Fig. 1d). The central excited Er can relax through surrounding defects (represented by black crosses) with a rate of $W_d(r)$ with r being the distance between Er and defects. It is the defect density distribution $\rho(r)$ and distance-dependent decay rate $W_d(r)$ that determine the final PL decay dynamics of the excited Er. The final line-shape can be deduced as a stretched exponential decay function (Kohlrausch's function),

$$\phi(t) = \phi_0 \exp[-(W_d t)^{\beta}] \quad (1)$$

in which ϕ_0 is the steady-state PL photoflux density and W_d is the effective PL decay rate that we will discuss later. The factor β represents the randomness of the system within the range between 0 and 1. $\beta = 1$ indicates a pure single exponential decay. For our system, β indeed barely changes at different temperatures (see SI-II, ESI†). In this article, we will use eqn (1) to analyze the transient Er PL dynamics. As shown in Fig. 1e, PL decay curves of the samples D_0, D_1 and S_1 can be finely fitted with this function. The β value of S_1 (0.7) is obviously higher than the other two samples (D_0: 0.56, D_1: 0.52). As described in Table 1, samples D_0 and D_1 were annealed at 950 °C for 5 min, while S_1 was treated at higher temperature for longer time (1100 °C for 30 min). Therefore, it is expected that a longer annealing time at higher temperature can help reduce the non-uniformity, or equivalently, increase the homogeneity of the system.

Carrier-mediated excitation model

Given the physical origin of the complex decay dynamics of excited Er ions, the dynamic energy transfer process is needed for further quantitative analysis of the Er PL. A widely accepted four-step model has been established for this process, as illustrated in Fig. 2.[9] In the first step (I), excess carriers are generated by external excitation. The excess carriers then start to relax to the conduction band minimum as the second step (II). In the third step (III), the excess carriers will relax through Shockley–Read–Hall (SRH) recombination *via* various defects introduced by implantation and then non-radiatively dissipate as heat or transfer to the surrounding Er ions exciting 4f electrons from $^4I_{15/2}$ to $^4I_{13/2}$. As to the final step (IV), the excited Er ions will relax to the ground state by emitting 1536 nm photons or non-radiatively by back transferring energy to the defects and surrounding. Clearly, the location of the defect energy level in the bandgap and the physical distance between the defects and Er ions have a profound implication in the four-step process. Logically, electrons trapped by EIDS are most likely to recombine non-radiatively, while those captured by ERDS are more likely to transfer their energy to excite Er ions as they are physically closer. The rate equations of ERDS-trapped carrier concentration n_{Er} and excited Er concentration N_{Er} can be expressed as,

$$\frac{dn_{Er}}{dt} = \eta_{trap} G - n_{Er}(W_{SRH} + W_{fd}) + N_{Er} W_{bt} \quad (2)$$

$$\frac{dN_{Er}}{dt} = n_{Er} W_{fd} - N_{Er} W_d \quad (3)$$

Eqn (2) and (3) correspond to steps III and IV in Fig. 2, respectively. η_{trap} is the probability of photo-generated carriers to be captured by ERDS, rather than EIDS, which should be a constant depending only on the defect distribution in the sample when they are highly degenerate (verified by Hall measurements in SI-V, ESI†). The average photo-carrier generation rate $G = \frac{(1-R)\varnothing_{in}}{L}$ in the Er-implanted region should be a constant at a fixed external pumping photoflux density ϕ_{in}. The (n, k) value at $\lambda = 405$ nm of our Er-implanted sample was measured to be (4.838, 0.732).[19] Accordingly, we have the reflectance $R = 0.43$ at 45° incidence and absorption coefficient $\alpha = 2.3 \times 10^5$ cm^{-1} with a corresponding skin depth of 44 nm. Thus, it is reasonable to assume that all transmitted light after reflecting at the air-silicon surface can be fully absorbed within the uniformly Er-implanted region with a thickness $L = 125$ nm (see SI-I, ESI†). W_{SRH}, W_{fd}, W_d, and W_{bt} are the SRH recombination rate *via* ERDS, Er forward excitation rate from ERDS, total PL decay rate and back-transfer rate, respectively. Note that we ignore the band-to-band radiative recombination in silicon since the band-edge emission for the Er-implanted sample is negligible as compared with the Er emission (see SI-VI, ESI†).

Temperature-dependent analysis

When photo-generated excess carriers are trapped by ERDS, they can recombine non-radiatively through the SRH process with a rate W_{SRH}, or transfer their energy to excite Er ions with a rate W_{fd}. Therefore, the energy transfer efficiency η_{ex} from ERDS to Er can be defined as

$$\eta_{ex} = \frac{W_{fd}}{W_{SRH} + W_{fd}} \quad (4)$$

The ratio of W_{SRH} and W_{fd} can be extracted by considering the temperature-dependency of steady-state PL emission photoflux density and transient decay rates.

At steady state, eqn (2) and (3) will be zero, from which the emission photoflux density ϕ_0 proportional to the concentration

Table 1 Basic information of samples D_0, D_1, and S_1

Sample	Er (cm^{-3})	O (cm^{-3})	B (cm^{-3})	Annealing method
D_0	8.7×10^{20}	1.6×10^{21}	0	DC (950 °C 5 min, 1000 K s^{-1} cooling rate)
D_1	8.7×10^{20}	1.6×10^{21}	7.7×10^{19}	DC (950 °C 5 min, 1000 K s^{-1} cooling rate)
S_1	8.7×10^{20}	2.0×10^{21}	7.7×10^{19}	SPE (1100 °C 30 min, natural cooling)

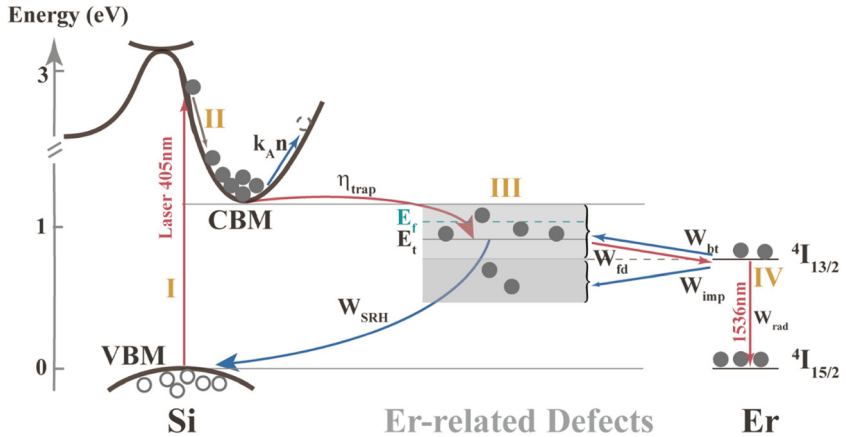

Fig. 2 Schematic diagram of energy transfer processes in Er-implanted silicon. Excess electrons are generated into the conduction band (CB, process I) under the excitation of an external pumping laser (λ = 405 nm). The excess electrons in the CB relax to the CB minimum (CBM, process II) and are then captured by Er-related defect states (effectively represented by E_t) with an efficiency η_{trap}, indicated by the red arrow from CBM to E_t. The trapped electrons relax from E_t and the valence band maximum (VBM) by transferring energy to the surrounding Er ions (W_{fd}, red arrow between defect states and Er ions) or non-radiatively (W_{SRH}, blue arrow). The excited Er ions can emit photons at 1536 nm with a radiative recombination rate W_{rad}. W_{bt}, W_{imp} and $k_A n$ are competitive decay rates corresponding to the energy back-transfer (up-conversion), impurity Auger effect (down-conversion) and free-carrier Auger effect, respectively.

of excited Er ions (N_{Er}) can be derived as (see SI-III, ESI† for derivation details),

$$\frac{1}{\phi_0} = A(W_0 W_{fd} + W_{SRH} W_d) \quad (5)$$

where A is a parameter proportional to the excitation photoflux density and the light collection efficiency of the PL system. The parameter can be canceled out after the normalization of ϕ_0.

When the excitation is turned off, excited Er ions will relax radiatively or through other non-radiative processes including the energy back-transfer, free-carrier and impurity Auger process. The back transfer process is a phonon-assisted

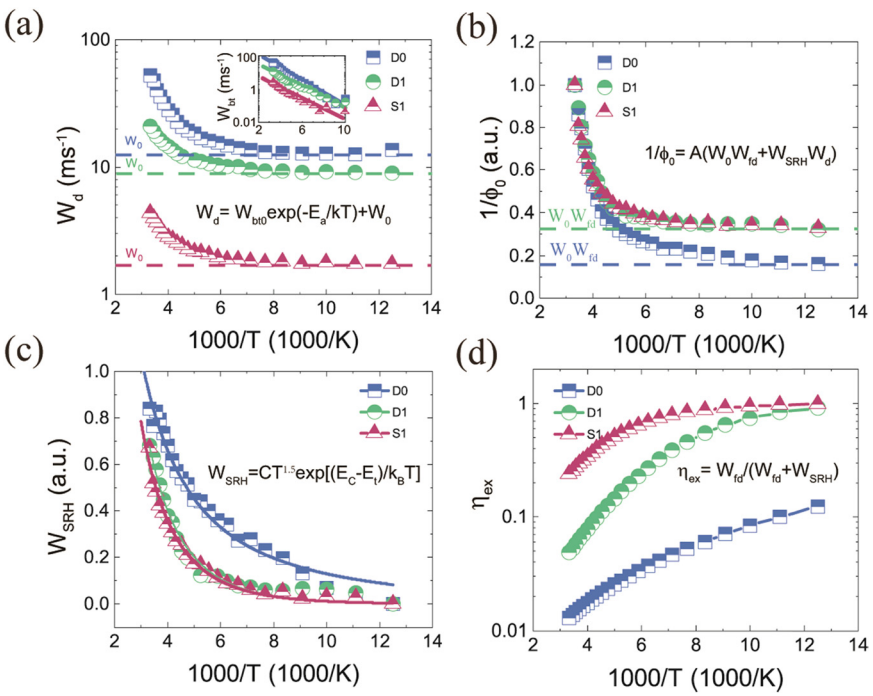

Fig. 3 Temperature-dependent PL measurements of the samples D_0, D_1 and S_1 at the pumping photoflux density ϕ_{in} of 5.5 × 10^{18} s^{-1} cm^{-2}. (a) PL decay rate W_d *versus* temperature T. The dashed lines represent the decay rate at a low temperature limit without the back-transfer process. The inset shows the pure back-transfer rate W_{bt} *versus* temperature after the subtraction of W_0. (b) Reciprocal of normalized emission photoflux density ϕ_0 *versus* 1000/*T*. The dashed lines indicate the low temperature limit of W_0W_{fd} without the temperature-dependency of energy back-transfer (W_{bt}) and SRH recombination (W_{SRH}). (c) Scaled Shockley–Read–Hall recombination rate W_{SRH} *versus* 1000/*T*. The solid lines are fitted curves using eqn (7). (d) Calculated excitation transfer efficiency *versus* 1000/*T* as defined by eqn (4) after obtaining the ratio between W_{SRH} and W_{fd}.

up-conversion process (W_{bt}), which can be expressed as the temperature-dependent term on the right of eqn (6) in which E_a is the activation energy of the back-transfer process, W_{bt0} is the back-transfer pre-factor, k_B is the Boltzmann constant and T is the absolute temperature. The other relaxation processes are temperature independent thus summarized as W_0 which will be discussed later in the power-dependent analysis section.

$$W_d = W_{bt} + W_0 = W_{bt0}\exp\left(-\frac{E_a}{k_B T}\right) + W_0 \qquad (6)$$

Using eqn (1) to fit transient PL signals at different temperatures for all three samples (D_0, D_1, S_1) as shown in Fig. 1e, we find the temperature dependency of the total decay rate W_d and photonflux density ϕ_0, which will be discussed in the following two sections, respectively.

Let us first focus on the total decay rate W_d as shown in Fig. 3a. Interestingly, W_d is correlated with temperature following exactly the theoretical eqn (6) for all three samples. Indeed, W_{bt} follows a simple exponential function of $1000/T$ (see the inset of Fig. 3a) when the temperature-independent base line W_0 is subtracted from W_d. By fitting eqn (6) to the experimental data as shown in Fig. 3a, we found the back-transfer activation energy E_a, energy back-transfer pre-factor W_{bt0} and the temperature-independent decay rate W_0. The results are summarized in Table 2. Note that the activation energy E_a should be regarded as an effective activation energy of all ERDS in the up-conversion back transfer process. From Table 2, we can see that E_a does not vary much (from 96 meV to 119 meV) However, the back-transfer pre-factor W_{bt0} decreases by one-order of magnitude when boron is introduced (from D_0: 3982 ms^{-1} to D_1: 464 ms^{-1} and S_1: 128 ms^{-1}), on comparing with the previous results.[20] This is likely caused by smaller electron cloud overlapping between 4f electrons and Si valence band electrons because boron atoms are more favorable than Er ions to bind with Si in the form of B–O–Si.[21] The introduction of boron dopants will reduce the direct interaction of Er and Si and thus lower the probability of energy back-transfer. This observation is consistent with the results obtained from the power-dependent analysis later. It is worthy of note that W_{bt0} of our sample S_1 is three-order smaller than the previously reported value (2×10^5 ms^{-1}), resulting in a back-transfer rate W_{bt} of only 2.5 ms^{-1} at room temperature, around 1/700 of a typical Er-implanted Si system.[20] This improvement can partly be explained by the optimized annealing and doping conditions (SI-II, ESI†). The other possible reason is the weaker Er-Si (valence band) coupling due to the much higher Er, O and B concentrations in our samples. The chances of Er directly binding with B and O are higher.

Now, let us look at the emission photoflux density ϕ_0. For simplicity, ϕ_0 is normalized to the value at 80 K in the further analysis. To use eqn (5) to guide our analysis, we made an Arrhenius plot of $1/\phi_0$ (Fig. 3b). The pre-factor A in eqn (5) is eliminated after the normalization. For the first term $W_0 W_{fd}$, W_0 is the relaxation rate of excited Er ions for the temperature-independent relaxation paths other than back transfer (see later discussions in the power-dependent analysis section); W_{fd} is the forward energy transfer rate from ERDS to Er ions, which is a down-conversion process and therefore also temperature independent. Clearly, the complicated temperature dependence of $1/\phi_0$ comes from the second term, a multiplication of W_d and W_{SRH}.

After deducting the temperature dependent W_d (see Fig. 3a) from $1/\phi_0$, we found amazingly that W_{SRH} for all three samples can be nicely fitted with the standard SRH trap-assisted recombination theory eqn (7) after a proper reformatting (see SI-IV, ESI†), as shown in Fig. 3c.

$$W_{SRH} = \frac{AN_c}{n_0^2}\exp\left(-\frac{E_c - E_t}{k_B T}\right) \qquad (7)$$

in which A is the constant related to defect density, minority carrier capture coefficient and photo-generated carrier concentration, which are fixed as demonstrated in SI-IV (ESI†), Nc is the effective density of states function in the conduction band which is proportional to $T^{3/2}$, n_0 is the electron concentration, E_c is the conduction band edge and E_t represents the effective position of ERDS. Note that n_0 is nearly independent of temperature as all the samples are degenerate (see SI-V, ESI†).

For this reason, we conclude that the Er PL transient decay in our samples can be reliably described by the equations presented above. From the fittings, we extracted E_c–E_t in Table 2. Combining with the extracted E_a in the previous

Table 2 Key parameters for samples D_0, D_1, S_1 with ϕ_{in} of 5.5×10^{18} s^{-1} cm^{-2} at 300 K

		Sample		
Parameters (unit)	Physical meaning	D_0	D_1	S_1
E_a (meV)	Activation energy in the back-transfer process	119	96	102
E_c–E_t (meV)	Energy difference between CBM and ERDS at room temperature	3.7	30.6	29.6
W_{bt0} (ms^{-1})	Energy back-transfer pre-factor	3982	464	128
W_{bt}@300 K (ms^{-1})	The energy back-transfer rate	38.9	11.1	2.5
W_0 (ms^{-1})	PL decay rate without back-transfer	13.5	9.4	1.8
W_{rad} (ms^{-1})	The radiative recombination rate of Er[17]	0.5		
N_{tt} ($\times 10^{19}$ cm^{-3})	Optically active Er concentration	1.23 ± 0.33	2.16 ± 0.19	2.02 ± 0.07
σ ($\times 10^{-16}$ cm^2)	Effective excitation cross section	2.15 ± 0.67	1.03 ± 0.11	0.58 ± 0.04
k_A/k_l (cm^3)	Effective free-carrier Auger coefficient	1.46×10^{-20}	2.83×10^{-21}	3.78×10^{-22}
$(1-R)\phi_{in}k_A/lk_1$ (ms^{-1})	The free-carrier Auger recombination rate caused by photo-generated electrons	3.67	0.71	0.09
W_{imp} (ms^{-1})	The impurity Auger recombination rate	9.33	8.19	1.21
η_{ex}	Energy transfer efficiency	0.014	0.05	0.22
η_{PLQY}	The photoluminescence quantum yield	6.7×10^{-4}	1.3×10^{-3}	4.5×10^{-3}

section, we found that all our samples endure a bandgap narrowing effect ($E_a + E_c - E_t + h\nu_{1536nm} < E_g$), which is reasonable under such high dopant concentration.[22]

Finally, let us return to eqn (4). The variable W_{fd} can be retrieved from the temperature-independent term W_0W_{fd} as shown in Fig. 3b with W_0 obtained from fittings shown in Fig. 3b (see SI-VI, ESI†). Therefore, the energy transfer efficiency η_{ex} (Fig. 3d) from ERDS to Er can be found from the given W_{fd} and temperature-dependent W_{SRH} as shown in Fig. 3c. We can see that η_{ex} approaches 1 as the temperature decreases, and that the sample S_1 has the least temperature dependent effect, resulting in the highest energy transfer efficiency of 21.6% at room temperature.

Power-dependent analysis

When the pumping power is large enough to excite most of the Er ions, the photo emission starts to be limited by the total number of ground state Er ions and therefore becomes saturated. In this case, the excitation rate of Er ions is not equal to $n_{Er}W_{fd}$, the first term in eqn (3). Instead, it should be proportional to the amount of unexcited Er and pumping photoflux density. Therefore, eqn (3) should be rewritten as

$$\frac{dN_{Er}}{dt} = \sigma\phi_{in}(N_{tt} - N_{Er}) - N_{Er}W_d \quad (8)$$

in which σ is the effective excitation cross section, a parameter to characterize the ability of Er ions to capture photons. N_{tt} is the total optically active Er concentration and ϕ_{in} is the pumping photoflux density at 405 nm. The steady state solution is

$$N_{Er} = \frac{\sigma\phi_{in}/W_d}{1 + \sigma\phi_{in}/W_d}N_{tt} \quad (9)$$

When the external pumping is high enough ($\sigma\phi_{in}/W_d \gg 1$), nearly all optically active Er ions are excited.

Now, we use eqn (1) to fit PL transient curves at different pumping photonflux density ϕ_{in} at room temperature. The emission photoflux density ϕ_0 and decay rate W_d *versus* ϕ_{in} can be obtained for the three samples. Previous analysis was based on normalized ϕ_0. Here, the absolute values of the emission photoflux density ϕ_0 of the three samples are measured in order to obtain their PLQYs (Fig. 4c). A common strategy is to place our samples in an integrating sphere to collect all the emitting photons. However, due to the high attenuation of our integrating sphere and the low responsivity of the photodetector, we choose to calculate the integrated photoflux density of our sample by calibrating with a commercial LED (Hamamatsu, L12509-0155G, 1550 nm) with known External Quantum Efficiency (EQE). In order to get a reliable estimation, the LED was chosen to emit at 1550 nm (close to the Er emission peak) and radiate in a similar far-field pattern with our samples (see SI-VIII, ESI†). During the calibration process, our samples and LED are placed at the same position on the sample holder, which implies equal collection efficiency in our system. Finally, the emission photoflux density of our sample can be obtained after extracting the collection efficiency of our system obtained from LED measurements (for details, see SI-VIII, ESI†). The corresponding PLQYs (Fig. 4c) were further calculated by dividing the light extraction efficiency (~2%) simulated with the Lumerical Finite Difference Time Domain (FDTD) module. Then, ϕ_0 can be converted into excited Er concentration N_{Er}. N_{Er} *versus* ϕ_{in}/W_d values for the three samples are plotted in Fig. 4a and fitted with eqn (9), from which we extract the excitation cross section σ and total optically active Er concentration N_{tt} as summarized in Table 2. It is intriguing that N_{tt} does not vary much among the three samples, and that the highest optically active Er concentration is about 2×10^{19} cm^{-3} (~2.5% of all implanted Er dopants). Although the active rate 2.5% is not giant, the absolute Er concentration in the Er-implanted silicon sample is a record-high value (two-order higher than the calibrated value in MBE-grown Er:Si, 1.3×10^{17} cm^{-3} [23]). Besides, if the absorption/emission cross section (5×10^{-19} cm^2) of Er is appropriately estimated by Lourenço, M. A. *et al.*,[12] the net optical gain in such system will be ~11 cm^{-1} assuming the maximum population inversion. However, for the effective excitation cross section, the sample S_1 (with boron dopants) has the smallest excitation cross section of 5.8×10^{-17} cm^2, about a quarter of the sample D_0. This phenomenon is consistent with the weaker Er–Si coupling

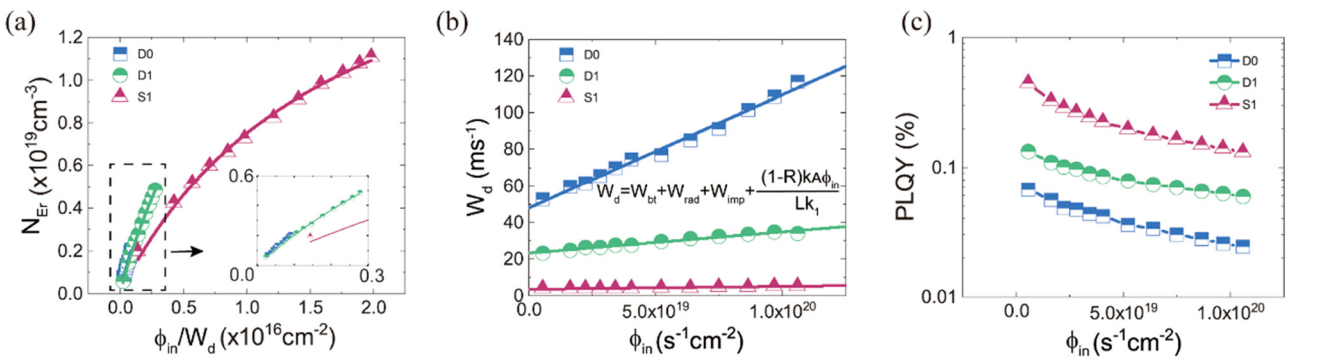

Fig. 4 Power-dependent photoluminescence measurements for the samples D_0, D_1, S_1 at 300 K. (a) Excited Er concentrations N_{Er} *versus* ϕ_{in}/W_d along with the fitting curves (solid lines) using eqn (9). The inset shows the enlarged curves for samples D_0 and S_0. (b) PL decay rate W_d *versus* pump photonflux density ϕ_{in}. The solid lines are linear fitting results using eqn (10), corresponding to the free-carrier Auger effect. (c) Calibrated PLQY as a function of pumping photoflux densities ϕ_{in}.

for samples with boron predicted previously in the temperature-dependent analysis.

The free-carrier Auger effect can be revealed from the power-dependence of the PL decay rate W_d. W_d *versus* ϕ_{in} values for the three samples at room temperature are shown in Fig. 4b. We can see that W_d increases linearly with ϕ_{in}. It is known that the relaxation process of excited Er ions can radiatively emit photons or non-radiatively excite the electrons in the Si valence band (back-transfer process) and conduction band as well as defect states in the bandgap (impurity Auger effect). The free-carrier Auger rate is proportional to the electron concentration n with coefficient k_A. As a result, the total decay rate W_d as discussed in previous eqn (6) at a specific temperature can be expressed as a more thorough form in eqn (10).

$$W_d = W_{bt} + W_{rad} + W_{imp} + k_A n \quad (10)$$

where W_{bt} is the back-transfer rate that can be calculated through the previous temperature-dependent model, W_{rad} is the radiative recombination rate of Er ions which can be found from the literature as 0.5 ms^{-1},[17] W_{imp} represents the impurity Auger process in which Er ions transfer the relaxation energy to electrons on various defect states. $k_A n = k_A(n_0 + \Delta n)$ is the free-carrier Auger recombination rate in which n_0 is the equilibrium electron concentration and Δn is the photo-generated excess electron concentration. k_A is a constant measuring the energy transfer rate from an excited Er to one free-moving electron. We would have $\Delta n \gg n_0$ at relatively high excitation intensities and therefore $k_A n \approx k_A \Delta n$ in which the excess carrier concentration Δn is correlated with the excitation photoflux density ϕ_{in} as $\Delta n = \frac{1-R}{Lk_1}\phi_{in}$ with R being the reflectance, L being the absorption length and k_1 being the SRH recombination rate *via* both EIDS and ERDS. Therefore, the terms on the right side of eqn (10) are all independent of the excitation power except for the last one which is linear with the excitation power, consistent with the experimental observation as shown in Fig. 4b. The slope of the linear correlation is $(1 - R)k_A/(Lk_1)$ with the reflection coefficient R = 0.47,[24,25] and the absorption length L = 125 nm at the incident wavelength of 405 nm. The intercept at the y axis is the sum of power-independent rates W_{bt}, W_{rad} and W_{imp} in eqn (10) in which W_{bt} at 300 K was previously found from Fig. 3c and W_{rad} can be found from the literature as 0.5 ms^{-1}.[17] The extracted effective Auger coefficients k_A/k_1 and W_{imp} are listed in Table 2. We can see that the k_A/k_1 values of boron-optimized samples D_1 and S_1 are around 1/5 and 1/40 of sample D_0, resulting in free-carrier Auger recombination rates of 0.71 and 0.09 ms^{-1} at room temperature (pumping ϕ_{in} 5.5 × 10^{18} s^{-1} cm^{-2}), comparable or even lower than the radiative recombination rate of Er ions (0.5 ms^{-1}). In this case, the radiative efficiency W_{rad}/W_d of excited Er ions will reach the maximum of $W_{rad}/(W_{bt} + W_{rad} + W_{imp}) \approx 12\%$. This value can be further improved to 16% if W_{imp} is zeroed out by defect passivation.

Previously, we have shown that the energy transfer efficiency from Er-related defects to Er ions is 21.6% at room temperature. We just found that the excited Er ions emit photons at a maximum rate of 12%. The referred PLQY should reach 2.6% (= 21.6% × 12%). However, the experimentally measured value is only 0.45% for our optimized sample S_1 as shown in Fig. 4c. This huge contrast in PLQY mainly comes from the impact of EIDS (surface states, lattice dislocations, *etc.*) which provide efficient pathways for excess electrons to recombine. As a result, only 17% (0.45/2.6) of the excess electrons will be captured by ERDS, *i.e.* the trap efficiency η_{trap} = 17%. If the EIDS are well passivated, we would expect that PLQY can reach 3.5% as η_{trap} will increase to 100% and the maximum radiative efficiency of Er ions will be $W_{rad}/(W_{bt} + W_{rad}) \approx 16\%$ (discussed above).

Conclusion

In conclusion, we used a stretched-exponential function to describe the PL behaviors of Er in Si. By tuning the dopants' concentrations and annealing conditions, the highest PLQY of 0.45% is obtained for the boron-doped sample with the record high optically active Er concentration of 2 × 10^{19} cm^{-3} in crystalline silicon. After analysis using the Er–Si coupling model, an energy transfer efficiency of 21.6% from ERDS to Er ions is obtained for the boron-optimized sample. When the EIDS is properly passivated, the excited Er ions will have a radiative efficiency of 16%. This implies that Er/O/B doped silicon will reach a maximum PLQY of 3.5% at room temperature. Hydrogen is a good candidate for passivation, which will be investigated in detail in our future research.

Experimental section

Sample preparation

Float zone (FZ) intrinsic Si(100) wafers (Resistivity: ≥10 kΩ cm; Thickness: 500 ± 20 μm; Suzhou Resemi Semiconductor Co., Ltd, China) were first implanted with Er, O, and B ions at the Ion Beam Center, Helmholtz Zentrum Dresden Rossendorf (HZDR), Germany. Implantation parameters are listed in the ESI† (see SI-I) to obtain uniform distributions of Er, O and B. Two types of samples were compared. One with only Er/O implantations while the other contains Er/O/B. For each type, two annealing methods were applied. One is the deep cooling (DC) technique with configuration and annealing conditions described in ref. 10. The other annealing method is solid phase epitaxy (SPE). The samples were placed in a quartz boat with sufficient distances. Firstly, the temperature of the Muffle furnace (Lindberg/BlueM) was increased and kept at 1100 °C. Then, the quartz boat was pushed into the furnace using an ion rod and annealed for 30 minutes. Finally, the boat was pulled out of the furnace and cooled down to room temperature. An N_2 atmosphere is guaranteed in this whole process.

Photoluminescence measurement

The samples were characterized using a photoluminescence (PL) spectrometer (Edinburgh, FLS1000) system to obtain their steady-state spectrum as well as the transient dynamics. Light from a commercial 405 nm laser (c.w. LD, MLL-III-405, CNI,

Changchun, China) was incident at our sample with an angle of 45°. The emitting light first went through a high-pass filter (645 nm), which was used to eliminate the scattering noise caused by the pump laser. A liquid N_2-cooled near-infrared photomultiplier tube (NIR-PMT), accompanied by a grating was used to perform the steady-state spectrum scan. For transient measurements, the pumping laser was modulated by a pulse controller with a frequency of 500 Hz (pulse width 387 μs). The transient PL signals were constructed by integrating the photocounts of 8000 distinct time channels (time window 2 ms, time resolution 250 ns) in 60 seconds to obtain a sufficient signal-to-noise ratio.

Author contributions

Y. D. conceived the idea and supervised the research. H. L. and Y. D. wrote the manuscript and derived the theoretical equations. H. L. performed PL measurements and data analysis. U. K. conducted the ion implantation. F. Y. supported the PL measurements. A. M. discussed the theoretical issues and commented on the manuscript. All authors reviewed the manuscript.

Conflicts of interest

The authors declare no competing financial interest.

Acknowledgements

This work was supported by the ''Innovative Research Plan,'' Shanghai Municipality Bureau of Education (2019-01-07-0002-E00075) and the National Science Foundation of China (61904102). PL measurements were carried out at the Instrumental Analysis Center of Shanghai Jiao Tong University. The authors are grateful to the support for PL analysis by Dr. Ruibin Wang at Instrumental Analysis Center of Shanghai Jiao Tong University. Ion implantation was conducted at the Ion Beam Center (IBC), Helmholtz-Zentrum Dresden-Rossendorf, Germany.

References

1 J. Michel, *et al.*, *Erbium Doped Silicon for Light Emitting Devices*, Mrs Proceedings, 1996, vol. 422, p. 317.
2 Z. F. Krasilnik, Y. Y. Aleshkin, B. A. Andreey, O. B. Gusey, W. Jantsch and L. Y. Krasilnikoyaj, *et al.*, SMBE-grown uniformly and selectively-doped Si:Er structure for LEDs and lasers. *Towards the First Silicon Laser*, 2003, p. 10.
3 P. G. Kik and A. Polman, Erbium-Doped Optical-Waveguide Amplifiers on Silicon, *MRS Bull.*, 2013, **23**(4), 48–54.
4 A. Polman, Erbium implanted thin film photonic materials, *J. Appl. Phys.*, 1997, **82**(1), 1–39.
5 Y.-G. F. Ren, *Erbium Doped Silicon as an Optoelectronic Semiconductor Material*, 1994.
6 A. J. Kenyon, Erbium in silicon, *Semicond. Sci. Technol.*, 2005, **20**(12), R65–R84.
7 X. M. Wang, *et al.*, Fluorine-Enhanced Room Temperature Luminescence of Er-Doped Crystalline Silicon, *Adv. Photonics Res.*, 2022, **2200115**, 6.
8 D. T. X. Thao, C. A. J. Ammerlaan and T. Gregorkiewicz, Photoluminescence of erbium-doped silicon: Excitation power and temperature dependence, *J. Appl. Phys.*, 2000, **88**(3), 1443–1455.
9 P. G. Kiki, M. J. A. de Dood, K. Kikoin and A. Polman, Excitation and deexcitation of Er3+ in crystalline silicon, *Appl. Phys. Lett.*, 1997, **70**(13), 4.
10 H. Wen, *et al.*, Efficient Er/O-Doped Silicon Light-Emitting Diodes at Communication Wavelength by Deep Cooling, *Adv. Opt. Mater.*, 2020, **8**, 2000720, DOI: 10.1002/adom.202000720.
11 T. Gregorkiewicz and J. M. Langer, Lasing in Rare-Earth-Doped Semiconductors: Hopes and Facts, *MRS Bull.*, 2013, **24**(9), 27–32.
12 M. A. Lourenço, R. M. Gwilliam and K. P. Homewood, Extraordinary optical gain from silicon implanted with erbium, *Appl. Phys. Lett.*, 2007, **91**(14), 141122, DOI: 10.1063/1.2797975.
13 J. L. Benton, *et al.*, The electrical and defect properties of erbium-implanted silicon., *J. Appl. Phys.*, 1991, **70**(5), 2667–2671.
14 J. Palm, *et al.*, Electroluminescence of erbium-doped silicon, *Phys. Rev. B: Condens. Matter Mater. Phys.*, 1996, **54**(24), 17603.
15 F. Priolo, *et al.*, The erbium-impurity interaction and its effects on the 1.54 μm luminescence of Er3 + in crystalline silicon., *J. Appl. Phys.*, 1995, **78**(6), 3874–3882.
16 N. Q. Vinh, *et al.*, Concentration of Er^{3+} ions contributing to 1.5−μm emission in Si/Si:Er nanolayers, *Phys. Rev. B*, 2007, **76**(8), 085339, DOI: 10.1103/PhysRevB.76.085339.
17 F. Priolo, *et al.*, Excitation and nonradiative deexcitation processes of Er3 + in crystalline Si, *Phys. Rev. B: Condens. Matter Mater. Phys.*, 1998, **57**(8), 4443–4455.
18 S. Coffa, *et al.*, Temperature dependence and quenching processes of the intra-4f luminescence of Er in crystalline Si, *Phys. Rev. B: Condens. Matter Mater. Phys.*, 1994, **49**(23), 16313–16320.
19 M. F. S. Joseph Klafter, On the relationship among three theories of relaxation in disordered systems, *Proc. Natl. Acad. Sci. U. S. A.*, 1996, **83**, 4.
20 N. Hamelin, *et al.*, Energy backtransfer and infrared photoresponse in erbium-doped silicon p–n diodes, *J. Appl. Phys.*, 2000, **88**(9), 5381–5387.
21 D. L. Griscom, G. H. Sigel and R. J. Ginther, Defect centers in a pure-silica-core borosilicate-clad optical fiber: ESR studies., *J. Appl. Phys.*, 1976, **47**(3), 960–967.
22 M. Wang, *et al.*, Extended Infrared Photoresponse in Te-Hyperdoped Si at Room Temperature, *Phys. Rev. Appl.*, 2018, **10**(2), 024054, DOI: 10.1103/PhysRevApplied.10.024054.
23 B. A. Andreev, *et al.*, Luminescent properties of MBE-grown Si:Er/SOI structures, *J. Lumin.*, 2012, **132**(12), 3148–3150.
24 X. Zhao, *et al.*, Efficient Er/O Doped Silicon Photodiodes at Communication Wavelengths by Deep Cooling, *Adv. Mater. Technol.*, 2021, **6**(7), 2100137, DOI: 10.1002/admt.202100137.
25 N. Q. Vinh, *et al.*, The Auger process of luminescence quenching in Si/Si:Er multinanolayers, *J. Phys.: Condens. Matter*, 2005, **17**(22), S2191–S2195.

